PHYSICAL REVIEW B **110**, 075404 (2024)

Adsorption and electronic structure of submonolayer Ca on Ag(111)

Heeseon Lim,[1] Yanan Wang,[2] Namitha Ann James,[1] Hongli Guo,[3,4] Jin Zhao,[1,4] and Hrvoje Petek[1,*]
[1] *Department of Physics and Astronomy, University of Pittsburgh, Pittsburgh, Pennsylvania 15260, USA*
[2] *Songshan Lake Materials Laboratory, Dongguan, Guangdong 523808, China*
[3] *Department of Physics and Astronomy, California State University Northridge, Northridge, California 91330-8268, USA*
[4] *Department of Physics and ICQD/Hefei National Research Center for Physical Sciences at the Microscale, University of Science and Technology of China, Hefei, Anhui 230026, China*

(Received 28 March 2024; revised 10 July 2024; accepted 11 July 2024; published 2 August 2024)

By frequency-time spectroscopy, microscopy, and electronic structure theory, we investigate the low coverage adsorption and electronic structure of Ca on an Ag(111) surface. The chemisorption of alkaline-earth Ca atoms starting from their closed $4s^2$ shell electronic configuration differs from that of the open ns^1 shell alkali-metal atoms because they retain some $4s$ electron charge and can involve hybridization with low-lying unoccupied $3d$ orbitals. Spectroscopic investigation of the unoccupied electronic structure of Ca on Ag(111) by three-photon photoemission (3PP) reveals the electronic states with dominant $3d$-orbital character, as confirmed by electronic structure theory. Coverage-specific spectral features enable attribution to two distinct chemisorption phases at submonolayer coverages, which are confirmed at the atomic scale by scanning tunneling microscopy and spectroscopy measurements. Furthermore, time-resolved 3PP spectroscopy reveals a resonant two-photon transition between occupied (~-0.3 eV) and unoccupied (~2.7 eV) states with dominant s- and d-orbital character. Interferometric time-resolved measurements probing this resonance reveal a dephasing time of ~21 fs and population lifetime of ~52 fs for the transiently populated d-like state at ~2.7 eV above E_F. Contrary to alkali-metal atom chemisorption, the characteristic development of the chemisorption and electronic structure of Ca reveals the importance of Ca adsorbate and Ag substrate interactions that cause a low-coverage atomic condensation into compact islands. Discovery of the long-lived d-character state informs on the catalytic and optoelectronic applications of the alkaline-earth element Ca.

DOI: 10.1103/PhysRevB.110.075404

I. INTRODUCTION

The structural and optical and/or electronic properties of single-atom adsorption on metals defines surface chemical and physical properties. The chemisorption of single atoms on a metal substrate modifies the local composite electronic properties via hybridization of atomic, electronic orbitals and charge transfer. As the most electropositive elements, the alkali-metal and alkaline-earth (AE) metals are some of the simplest species for describing the transformation of electronic structure upon chemisorption, which nevertheless exhibit complex interactions. Alkali-metal atoms have been extensively studied to describe the adsorption behavior and the consequent electronic structure modification that is induced by the interaction of their single (s^1) valence electron with supporting surfaces. This has made the adsorption of alkali-metal atoms on various metal surfaces the primary theoretical and experimental topic since the beginning of surface physics [1–8]. Such studies have concluded that alkali-metal atoms chemisorb on metals by dominantly transferring their single s electron, leading to characteristic alkali-metal-induced spectral features above the Fermi level (E_F). Spectroscopic studies by multiphoton photoemission (mPP) spectroscopy and electronic structure theory have attributed these states to hybridization of their s and p orbitals [9–16].

Despite the fundamental role of alkali-metal atoms in understanding of surface physics, only a few studies have been extended to exploring the complexities of electron correlation in AE atoms that is associated with their closed s^2-orbital electronic configuration [15,17]. As a simple model of electron correlation, significant studies have been performed on the electronic structure of Be metal, for which the d orbitals are too high in energy to play a significant role [18–20]. AE atoms exhibit some similarities to alkali-metal atoms, such as their low ionization potentials, and transfer of nearly one electron upon chemisorption, which consequently decreases work functions of the composite surfaces [21]. Like alkali-metal atoms, they also form intercalation compounds with graphite, and are found in an important family of d-wave superconductors, where their easy charge donation, electron-phonon interaction, ionic interactions, and particularly low-lying d orbitals play important roles in imparting superconducting properties [22–25]. Whereas alkali-metal atoms at submonolayer coverages chemisorb predominantly into hexatic liquid overlayers that are defined by dipole-dipole repulsion [7,26–29], similar structural studies of AE atoms on various metal surfaces, by contrast, have revealed the importance of the interatomic as well as the atom-substrate interactions that lead to

---

[*] Contact author: petek@pitt.edu

island formation even at a fraction of a monolayer (ML) coverage [30–32]. Unlike alkali-metal atoms, the higher atomic number (Z) AE atoms, e.g., calcium (Ca), strontium (Sr), and barium (Ba), gain additional complexity in their electronic structures in their $(n-1)d$ orbitals being close in energy to their valence ns orbital. This enables facile s-p/d hybridization that impacts their chemical and electronic properties in molecular and solid-state forms [33–37]. Such hybridization can give rise to appreciable d-orbital character in the bonding properties of AE solids, contributing to their cohesive energy, as well as defining the properties of their low-lying electronic states [21]. Furthermore, it has been suggested that high-Z Ca, Sr, and Ba AE atoms may engage their d orbitals in chemical bonding to other adsorbates, enabling them to act as "honorary transition metals" [35,38–43]. The d-orbital participation in chemical properties is notably evident in the calcium carbonate cycle where the interaction with CO_2 to form $CaCO_3$ is thought to act as negative feedback on atmospheric CO_2 accumulation [44,45]. Ca, being one of the most earth-abundant metals, makes its environmental chemistry a significant potential sink for atmospheric CO_2 sequestration. Moreover, it has been proposed that AE solids can exhibit topological nodal line semimetal band structures involving overlap between dispersive bands of their ns and $(n-1)d$ orbitals [18,46]. These complex electronic interactions and high chemical activity invite closer scrutiny of the physical and chemical properties of chemisorbed AE atoms with high Z, and in particular how the proximity of $(n-1)d$ orbitals affects their intrinsic structural, chemical, optical, and electronic properties.

Calcium stands at the boundary between s- and d-orbital blocks in the periodic table. While the $3d$ orbitals of free Ca atoms are not occupied in the atomic ground state, in the metallic form or when chemisorbed on a metal surface, hybridization between the $4s$ and $3d$ orbitals must occur for Ca-Ca bonds to form, leading to an observable d-electron-like character near E_F [21,34,47,48]. Here, we investigate the fundamental adsorption behavior of Ca on Ag(111) at submonolayer coverage and explore its distinct character with respect to alkali-metal atoms. We examine the low-energy excitations of chemisorbed Ca atoms by mPP ($m = 3$) spectroscopy and find excitations of electronic states having strong d-orbital character, which are further confirmed by coverage-dependent scanning tunneling microscopy (STM) and scanning tunneling spectroscopy (STS), and density functional theory (DFT). Three-photon photoemission (3PP) spectroscopy, in conjunction with DFT calculations, reveals a partially occupied $4s$ state of Ca appearing just below E_F and two unoccupied states of different Ca phases with predominant $3d$-orbital character. This suggests that chemisorbed Ca exists in valance of $+1$ in chemisorbed form, retaining approximately one valance electron. In-depth analysis of the spectral properties provides evidence for the crucial contribution of the $3d$-orbital character even in the initial stage of condensation causing aggregation starting at ~0.05 ML coverages. Finally, we employ the interferometric time-resolved 3PP spectroscopy (ITR-3PP) to explore the photoinduced electron dynamics in resonant excitation. Resonant two-photon electronic transition populating an empty $3d$ state at ~2.7 eV measures a ~21-fs dephasing time and ~52-fs excited state population lifetime, suggesting the possibility of coherent optical manipulation of optoelectronic and photocatalytic properties of Ca-atom-decorated metal surfaces.

II. METHODS

A. Experiment

Experiments are performed under ultrahigh vacuum (UHV) conditions with a base pressure of $<3 \times 10^{-10}$ mbar. A clean Ag(111) surface is prepared by several cycles of sputtering and annealing. Ca atoms are evaporated onto prepared Ag(111) under a constant flux by Ohmic heating of a commercial getter source (AlfaVakuo e.U.). During the evaporative deposition, the pressure does not exceed $\sim 6 \times 10^{-10}$ mbar. The sample preparation and measurements are conducted in the same UHV chamber without exposure to air. For static mPP spectroscopy, tunable excitation light ($\hbar\omega_L = 1.33 - 1.82$ eV) with ~20-fs laser pulse is generated in a noncollinear optical parametric amplifier (NOPA) pumped by the second harmonic of a Clark MXR Impulse laser oscillator-amplifier system. The excitation laser is operated at a 1-MHz repetition rate. The p-polarized excitation light pulses are focused onto the sample surface at an incident angle of 45°. Photoemitted electrons are collected by a hemispherical energy analyzer (SPECS Phoibos 100) with an acceptance angle of ±15° and electron counting delay line detector. The detector records photoelectron counts versus photoelectron energy (E_{fin}) relative to E_F and parallel momentum ($k_\parallel$). For interferometric pump-probe delay scanning, two identical pump and probe pulses are generated in a Mach-Zehnder interferometer. The relative pulse delay, τ, is interferometrically scanned while recording three-dimensional $E_{\text{fin}}(k_\parallel, \tau)$ interferograms in ~100-as scan delay steps [49]. Low-temperature (LT) STM and STS measurements are performed in a separate Omicron LT-STM vacuum chamber to characterize the sample chemisorption and electronic structure with atomic resolution. STM images are obtained at ~77 K in the constant current mode. STS measurements are performed by a lock-in technique with a sinusoidal modulation voltage. Specific sample bias voltages are reported in each figure. The negative and positive bias tunneling probes the occupied and unoccupied states of the Ca/Ag(111) surface, respectively.

B. Theory

DFT calculations of the crystalline lattice and electronic structure of Ca on the Ag(111) surface are performed using the Vienna *Ab initio* Simulation Package (VASP) [50,51]. The Perdew-Burke-Ernzerhof exchange-correlation functional [52] along with projector-augmented wave potentials [53] is employed. The atomic geometry of each superlattice is optimized until the residual force on each atom is below 0.01 eV Å^{-1}. A 20-Å vacuum layer is included in the supercells to model surfaces in periodic intervals. For the static electronic structure calculations, only the Γ point of the first Brillouin zone is used, as it is found to be sufficient. The dimension of the hexagonal supercell for the close-packed monolayer of Ca on Ag(111) is $a = 11.64$ Å, with a Ca layer of $3 \times 3 \times 1$ and Ag(111) layers of $4 \times 4 \times 4$.

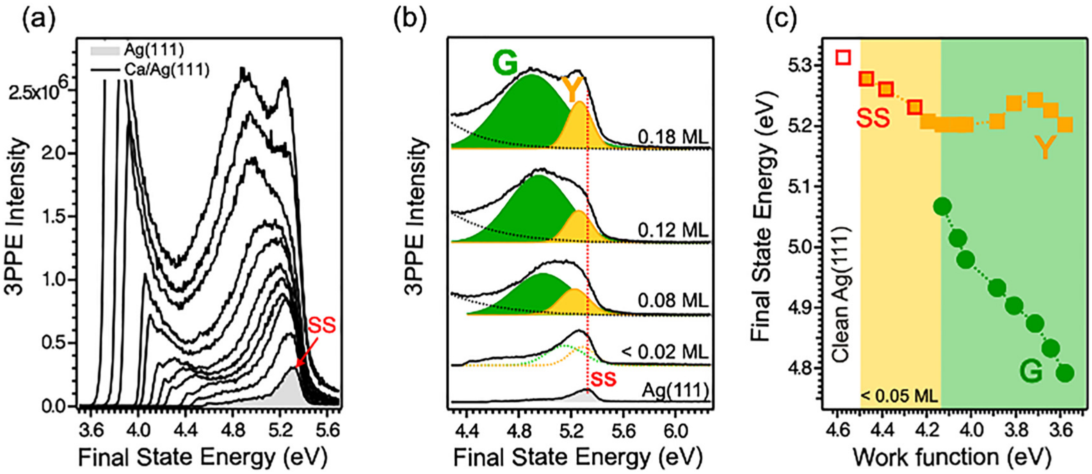

FIG. 1. Ca-coverage-dependent 3PP spectroscopy on Ag(111). (a) 3PP spectra obtained by $\hbar\omega_L = 1.79$ eV excitation for increasing Ca coverage on Ag(111); Ca atom is deposited until the work function decreases by $\Delta\phi = -1$ eV, whereupon the lower-nonlinear-order 2PP signal starts to dominate. (b) Deconvolution of the spectra into two Ca state-induced Gaussian peaks, labeled Y (yellow) and G (green), and the hot electron 2PP background (black dotted line) at four different Ca coverages (<0.02, 0.08, 0.12, and 0.18 ML). (c) The change of E_{fin} for the Ca-induced peaks Y and G versus work function energy at different coverages. The peak energy of Y is not resolved from the SS of Ag(111) at low coverages of <0.05 ML. The broad peak, G, appears clearly above ~0.05 ML and is highly sensitive to the coverage.

III. RESULTS

A. 3PP and STM spectroscopy of Ca adsorption on Ag(111)

We first investigate the 3PP spectral features induced by Ca adsorption on an Ag(111) surface at submonolayer coverages ($\leqslant$~0.18 ML). Note that we define a ML as one Ca atom per Ag atom, which has a surface density of 1.38×10^{15} atoms/cm^2. Because the atomic diameter of Ca (0.394 nm) is larger than that of Ag (0.288 nm), a full, close-packed layer of Ca on Ag(111) is expected at a coverage of ~0.53 ML, according to the above definition. Representative 3PP spectra in Fig. 1(a) are obtained during sequential deposition of Ca on Ag(111) using excitation at $\hbar\omega_L = 1.79$ eV. The gray shaded spectrum shows the initial 3PP spectrum of the clean Ag(111) surface; it is defined by a work function of ~4.57 eV and a peak due to the partially occupied Shockley surface state (SS), which appears at $E_{\mathrm{fin}} \sim 5.3$ eV. Other features such as the image potential states or the bulk *sp* band of Ag(111) are not observed because they can only appear in higher nonlinear order four-photon photoemission (4PP) [49,54,55]. While the excitation laser power is kept low, Ca adsorption greatly increases photoelectron counts in 3PP and continuously decreases the work function (ϕ) due to the adatom charge-transfer-induced dipole moment between Ca and Ag(111), as described in Supplemental Material Fig. S1 [56] (see also Refs. [15,21,57–64] therein). To estimate the Ca coverage during its deposition, we monitor ϕ (Fig. S1 [56]) as it converges to a constant value of ~3.2 eV at ~0.5 ML. The asymptotic value of $\phi \sim 3.2$ eV corresponds to that of Ca film grown on Si(111) (~3.2 eV) and the theoretical value of the close-packed Ca monolayer (3.13 eV) [21,65,66].

As Ca is deposited, a peak just below the SS in 3PP spectra is substantially enhanced (peak Y), and another separate peak appears at an energy below Y ($E_{\mathrm{fin}} < 5$ eV; peak G). To characterize the new Ca-induced spectral features, in Fig. 1(b) we show fitting of the spectra at four different Ca coverages (<0.02, 0.08, 0.12, and 0.18 ML) to two Gaussian line shapes and a tailing exponential background attributed to hot electrons that are detected after deposition of the Ca overlayer [67]. Although the energy position of Y is very close to the SS of Ag(111), angle-resolved spectra in Fig. S2 [56] indicate that it is distinct from the SS in that its band is dispersionless, whereas the SS has a very low band mass of $0.39m_e$ (m_e is the free electron mass). Nevertheless, the two electronic features coexist and are likely to be related. Considering that the Y intensity increases with Ca coverage, and its coverage dependence is different from the alkali-metal-atom chemisorption-induced decrease in SS energy [15,68,69], we consider Y to have specifically a Ca-derived electronic origin. Based on the analysis in Fig. 1(b), the change of E_{fin} for Ca-induced peaks (Y and G) at $k_{||} = 0\,\text{Å}^{-1}$ is plotted against ϕ in Fig. 1(c). In the process of Ca deposition, the initial peak energy shifts are towards lower energy in accordance with the change of ϕ. This initial shift can be attributed to reduction of the surface potential, which reduces the energies of surface states that are defined by it. The shift becomes more pronounced as the state energy approaches the vacuum level. Such shifts are known from previous studies of deposition of alkali-metal and AE atoms onto noble metals [9–11,15,70].

The analysis of Ca-induced peaks Y and G allows a nuanced interpretation of Ca adsorption behavior on Ag(111). Figure 2(a) shows the work function change as a function of Ca coverage, where the x axis (coverage) is displayed in a logarithmic scale to show the difference in the initial work function drop at a rate of −11.56 eV/ML below ~0.05 ML. Above ~0.05 ML coverage, however, the work function change rate suddenly decreases to −2.16 eV/ML, while the peak G begins to appear. The rate change suggests that adsorption behavior of Ca changes above ~0.05 ML, such that the polarization of the surface per adsorbed Ca atom decreases (inset in Fig. S1(a) [56]). In Fig. 2(b), top and bottom data report the FWHM linewidth and final state energy (E_{fin}) as a function of Ca coverage for both peaks Y and G, respectively. In contrast to Y, which has a relatively constant E_{fin} and

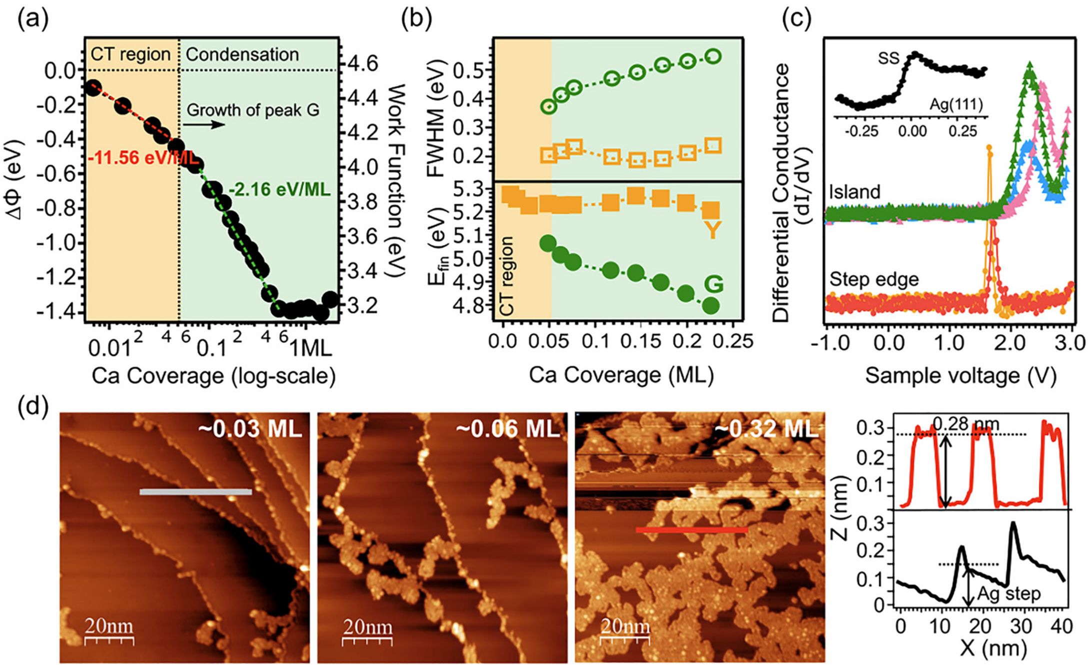

FIG. 2. Early stage Ca growth on Ag(111). (a) Work function change versus Ca coverage. The Ca coverage (note x axis in logarithmic scale; for linear scale, see Fig. S1 [56]). At the initial stage of growth, the work function dramatically decreases with a slope of −11.56 eV/ML, implying strong polarization at the atom-substrate interface (yellow shaded area). Above ∼0.05 ML, the work function slope changes to −2.16 eV/ML and peak G begins to appear. (b) The change of spectral properties [final state energies (E_{fin}; solid symbols) and full width at half maximum (FWHM; open symbols)] of Y and G as a function of Ca coverage at $\hbar\omega_L = 1.79$ eV in Fig. 1. (c) Differential conductance (dI/dV) spectra in the range of $V_s = -1$ to 3 V taken at two distinct Ca adsorption positions on Ag(111). The dI/dV measurement for Ca atoms at the step edges is performed at the interface between Ag and the Ca island, and the dI/dV spectrum for the Ca island is acquired from the center of the condensed Ca island. Bottom spectra (red and yellow): LDOS for Ca atoms adsorbed at the step edges. Top spectra (green, pink, and blue): LDOS for Ca islands. Inset: LDOS of the clean Ag(111). (d) Large-scale ($100 \times 100\,\text{nm}^2$) STM images at the different Ca coverages (∼0.03, ∼0.06, and ∼0.32 ML, respectively). Right: Line profiles along the gray line at ∼0.03 ML and the red line at ∼0.32 ML. All STM images are scanned at a sample voltage, $V_s = 2$ V, with a set current $I_{set} = 0.1$ nA at ∼77 K.

FWHM, G shows a decrease of E_{fin} by ∼0.3 eV at $\theta_{\text{Ca}} > 0.05$ ML, while its FWHM continuously increases with the coverages. This distinct behavior of E_{fin} and FWHM of peak G suggests energy stabilization and delocalization of electrons by band formation [71,72]. The $k_{\parallel}$ band dispersion of peak G in 3PP spectra (Fig. S2 [56]) supports that it forms a dispersive band defined by an effective mass $m_{\text{eff}} = (0.47 \pm 0.04)m_e$ whose energy and width are likely to be affected by the degree of in-plane band localization as well as disorder. The distinct spectral behavior of G reflects the unique nature of Ca adsorption compared to alkali-metal atoms on various noble metal surfaces. Unlike alkali-metal atoms, which experience repulsive dipole-dipole interactions hindering condensation into close-packed structures, Ca adsorption exhibits different character that favors island formation, because dipole-dipole repulsion is weak [9–11,26,73–75].

To provide further understanding, we record a series of LT-STM images of the dominant overlayer structures after the sequential Ca deposition at ∼300 K, as shown in Fig. 2(d). At initial Ca growth (∼0.03 ML), Ca atoms adsorb preferentially at the step edges or point defects on Ag(111). Such defects act as nucleation centers, leading to Ca island growth. As Ca coverage increases, Ca atoms coalesce into two-dimensional (2D) islands with irregular shapes having a uniform height of ∼0.28 nm [see a line profile in Fig. 2(d)]. A study of Ca on graphene reported a height of ∼0.27 nm for Ca monomers [76]. This similarity supports the conclusion that Ca atoms undergo layer-by-layer growth starting with 2D islands at the submonolayer stage. In addition, a clear contrast at the boundary between the step edges and the Ca islands is interpreted as evidence that a surface Ag-Ca alloy does not form at ∼300 K [77–79].

We also record dI/dV spectra of distinct structural features in Fig. 2(c). Although the irregular size and shape of Ca islands cause local density of states (LDOS) to depend on the measurement positions, two consistent features stand out: a broad peak with a position-dependent energy appears at ∼2.5 eV and a much sharper peak appears at ∼1.7 eV. Whereas the broad peak at ∼2.5 eV can be recorded at most Ca island areas, the position-dependent 1.7-eV feature is confined to Ca atoms specifically at step edges or point defects (see dI/dV mapping images in Fig. S3 [56]). From this we conclude that, at the early stage of growth, Ca atoms diffuse across terraces until they adsorb at stronger binding sites such as steps, kinks, and other defects, where they give rise to the sharp peak at ∼1.7 eV. At higher coverage, Ca atoms condense into small islands seeded by interaction with Ca atoms at the primary adsorbed sites. The interaction between Ca atoms forming islands dramatically reduces the net change in the work function at a higher coverage (>0.05 ML), as shown in Fig. 2(a) and

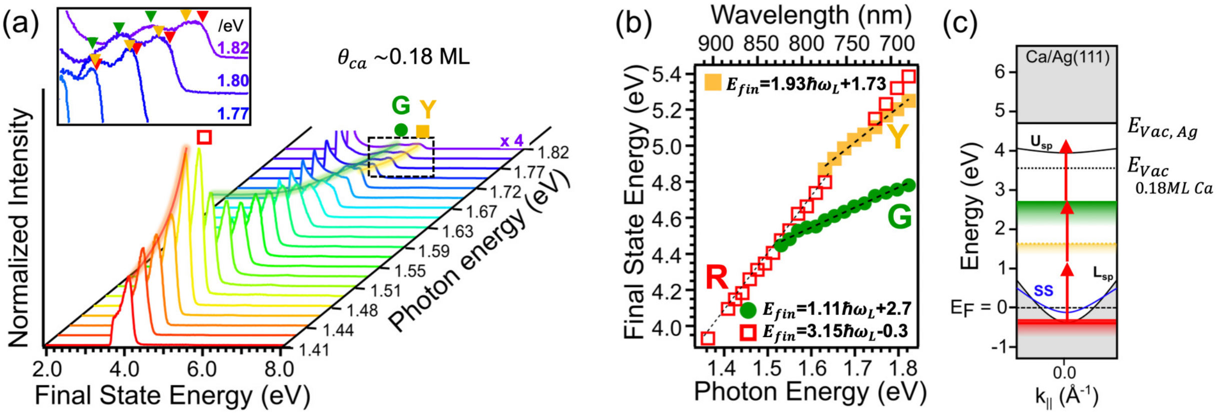

FIG. 3. Electronic structure of Ca on Ag(111). (a) Series of 3PP spectra for ~0.18 ML Ca on Ag(111) with *p*-polarized light in the range $\hbar\omega_L = 1.36 - 1.82$ eV. All spectra are normalized at the secondary electron cutoff (work function). Because the photon energy above ~1.8 eV is near the onset of 2PP, both spectra at 1.82 and 1.8 eV are multiplied by 4 to display the weaker 3PP spectral features. Inset: Enlarged spectrum near the Fermi edge in the dotted box for $\hbar\omega_L = 1.77 - 1.82$ eV. (b) Final state energy (E_{fin}) versus photon energy ($\hbar\omega_L$) measured in 3PP spectra. The slopes of 1.93 for Y and 1.11 for G are consistent with unoccupied states with binding energies (*y* intercept) of 1.73 and 2.7 eV above E_F, respectively. In (a) and (b), another spectral feature (red, denoted R) with a slope of 3.15 belongs to an occupied state with a binding energy of ~−0.3 eV below E_F. (c) The energy diagram of Ca-related states on the surface-projected electronic band structure of Ag(111). The red arrow shows two-photon resonant R→G excitation for $\hbar\omega_L = 1.48$ eV. This resonant excitation enhances the most intense 3PP signal in (a) at $E_{\text{fin}} = 4.33$ eV.

Fig. S1 [56]. Once Ca islands form, the broad peak appears at ~2.5 eV, but its energy and width reflect the inhomogeneity of the island structure.

To directly test the occupation of valence electrons on Ca atoms, we also measure the LDOS near E_F. Figure S4 [56] shows the measured LDOS of a clean Ag(111), Ca atom adsorbed at a defect and Ca island near E_F. Contrary to the LDOS of Ag(111) and Ca atom showing only a (modified) surface state feature of underlying Ag(111), the Ca island shows a broad LDOS feature across E_F centered at ~−0.25 eV, indicating valence electron occupation. Therefore, our analysis with STM and STS measurements suggests the two phases of adsorbed Ca: (1) the partially ionized Ca atoms on steps or defect sites at the initial growth (< ~0.05 ML) and (2) the 2D condensed Ca islands with a high occupied electron density. We also note that Ca single atoms are likely to be present on Ag(111) terraces, as necessary for the island growth, but are too mobile to image by STM at 77 K. Indeed, STM measurements at ~4.5 K reveal single Ca atoms on Ag(111) terraces (Fig. S4 [56]).

To correlate the spectroscopic and microscopic data, we investigate the electronic structure of Ca on Ag(111) by wavelength-dependent 3PP spectroscopy. The peak shift of spectroscopic features with $\hbar\omega_L$ enables assignment of peaks to the occupied or unoccupied states and defines their energy relative to E_F [80]. Figure 3(a) shows 3PP spectra normalized at the secondary electron cutoff (i.e., work function edge), where $E_{\text{fin}}(k_\|)$ spectra are drawn for $k_\| = 0\,\text{Å}^{-1}$ for increasing $\hbar\omega_L$. As $\hbar\omega_L$ is tuned from $1.36 < \hbar\omega_L < 1.82$ eV, the peaks Y and G participate in specific resonances revealed in 3PP spectra. According to $\hbar\omega_L$ dependence of the final state energies (E_{fin}) of these features in Fig. 3(b), the slopes of 1.93 ± 0.06 and 1.11 ± 0.03 identify states Y and G as being excited by two and one photon photoemission processes from unoccupied states with binding energies of 1.73 and 2.7 eV above E_F, respectively, given by their intercepts. The energy assignments of states Y and G are consistent with LDOS measurements by STS in Fig. 2(c), though the STS can give modestly different energies because of a tip-induced Stark effect [81]. In addition to Y and G, peak R is the dominant spectral feature for $\hbar\omega_L <$ ~1.5 eV, indicated by red symbols in Fig. 3(b); it has a slope of 3.15 ± 0.09 and intercept (binding energy) of −0.3 eV. For $\hbar\omega_L < 1.6$ eV peak Y disappears because the excitation photon energy is insufficient to populate it. In a 3PP process, a state with a slope of ~3 indicates excitation from an initial state below E_F. This suggests that a valence electron remains on Ca or is donated to the modified SS near Ca atoms in condensed islands on Ag(111), in agreement with STS measurement in Fig. S4 [56]. Investigation of Ba chemisorption on Cu(111) by single-photon photoemission has already reported that a valence electron remains just below E_F in agreement with a partial electron transfer to the substrate [15]. Therefore, our analysis with microscopic and spectroscopic tools is consistent with the previous study. Finally, based on the analysis of wavelength-dependent 3PP spectra for the entire excitation range ($1.36 < \hbar\omega_L < 1.82$ eV), the energy levels of three Ca-related states are drawn on the surface-projected band structures of Ag(111) in Fig. 3(c). Because the 3PP measurement produces an ensemble average value over the excitation beam <50 μm in diameter, an atomically nonuniform surface provides multiple features with inhomogeneous broadening that can be attributed to the different phases of Ca. Thus, we assert that the band structure in Fig. 3(c) contains two Ca unoccupied induced features: states G for the condensed Ca islands and state Y for Ca atoms decorating the Ag(111) step edges.

From this analysis, we conclude that Ca adsorption introduces an initial state (R) below E_F, from which the Y and G states are excited at specific photon energies. As the resonant excitation maximizes the photoelectron yields, a sharp increase of intensity at $\hbar\omega_L =$ ~1.48 eV establishes that two-photon resonance enhances transition from occupied state R to unoccupied state G. The resonant transition from R to Y is not obviously enhanced based on the photoemission yield at $\hbar\omega_L = \sim 1.75$ eV, although the inset in Fig. 3(a) displays their distinct spectral overlap at the same E_{fin}. This lack of enhancement can be attributed to the weak wave-function overlap between the delocalized R state over the Ag surface and the Y state originating from Ca atoms at the Ag step edge. In addition, the spectral feature of Y appears at the energy edge where both two-photon photoemission (2PP) and 3PP contribute to the signal, resulting in a low photoelectron intensity. This is further influenced by the inhomogeneous adsorption on the Ag(111) surface, which mainly consists of terrace areas with only a small portion of steps. Since photoelectron spectra measure the average signal from this inhomogeneous surface, the low intensity and the minimal enhancement at the resonance can be attributed to the relatively small number of Ca atoms adsorbed at the step edge.

B. The calculated electronic structure for Ca adsorption on Ag(111)

Next, we consider the DFT-calculated electronic structure of isolated and monolayer Ca on Ag(111) in relation to the observed electronic structure that is reported in the previous section. We specifically investigate how the *s*-*p*-*d* mixing affects Ca-atom aggregation on metal surfaces. Because the unfilled *d* orbitals of noninteracting single Ca, Sr, and Ba atoms are energetically closest to their filled *s* shell, and even below their *p* shell, upon chemisorption the *s*-*p*-*d* mixing is a strong factor for *d* orbitals becoming partially filled [40,48]. Thus, the participation of 3*d* orbitals affects the electronic, adsorption, and chemical structure of chemisorbed Ca [82–84].

The coverage and $\hbar\omega_L$-dependent 3PP spectra and STM and STS measurements identify two unoccupied states (Y and G) and one occupied state (R) depending on the phases of Ca chemisorbed on Ag(111) at submonolayer coverage. Comparison between the experiment and theory identifies the main orbital character of the Ca-induced spectral features. Figures 4(a) and Figs. S5 and S6 [56] show the DFT-calculated density of states (DOS) for a single Ca atom on Ag(111), and its *s*-, *p*-, and *d*-orbital components, respectively. In the Ca/Ag(111) (6 × 6) structure, there is minimal interaction among neighboring Ca atoms, so it is taken to represent the isolated atom electronic structure. Significantly, most of the prominent states for a single Ca atom near E_F possess a significant *d*-orbital character, while the *s* state is below E_F and experiences significant electron transfer to Ag(111) (see Fig. S5(a) [56]).

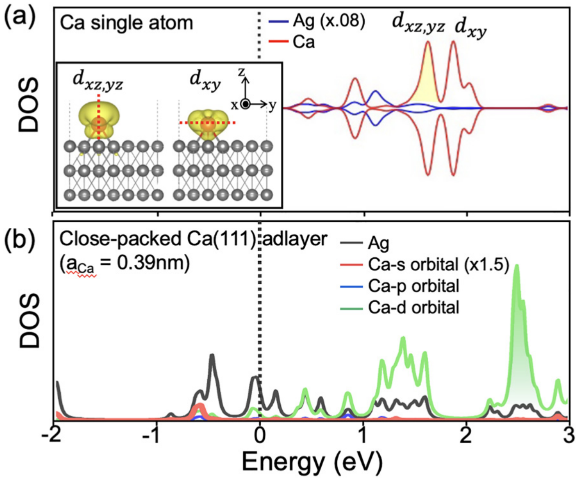

FIG. 4. Density functional theory (DFT) calculations. (a) DFT-calculated projected DOS of Ca single adatom on 6 × 6 Ag(111). Inset: The spatial orbital distributions of yellow shaded area denoted by $d_{xz,\,yz}$ at ∼1.7 eV. The gray spheres are Ag atoms of the substrate, and the red sphere is a single Ca adatom. The *z* axis is perpendicular to the surface. (b) DFT-calculated projected surface DOS of a close-packed Ca(111) layer on Ag(111) where the Ca-Ca bond length is 0.39 nm. The black curve shows the DOS of Ag(111), while the red, blue, and green are the Ca DOS curves decomposed into *s*-, *p*-, and *d*-orbital components, respectively.

For a Ca atom adsorbed on Ag(111) in Fig. 4(a), a sharp peak at ∼1.7 eV, which corresponds to the unoccupied state Y, has contributions from two degenerate states with dominant *d* character belonging to the d_{xz} and d_{yz} orbitals. The spatial orbital distributions at ∼1.7 eV depicted in the inset of Fig. 4(a) show that they lack surface normal nodal structure as expected for linear combinations of the d_{xz} and d_{yz} orbitals with some *s* and *p* character (σ symmetry). We note that the additional sharp feature at ∼1.9 eV belongs to an in-plane $3d_{xy}$ orbital (Fig. S5(b) [56]), which is oriented parallel to the surface. This feature has a node in the direction of the surface normal, resulting in the minimum intensity for normal emission such as π resonance of an alkali-metal-induced feature [16]. Although this state may be optically active, the photon energy range ($\hbar\omega_L = \sim 1.36$ to ~ 1.82 eV) that could be applied is insufficient to populate the $3d_{xy}$ state at its predicted energy of ∼1.9 eV. In our 3PP experiment, thus, we do not find evidence for the $3d_{xy}$ feature. The DFT-calculated DOS of a single Ca atom in Fig. 4(a) also does not provide clear evidence of the unoccupied state G at ∼2.7 eV. In Figs. 2 and 3, we find the distinctly different spectral features between two unoccupied states (Y and G) depending on Ca coverage, suggesting that a broad feature of state G at ∼2.7 eV can be specifically attributed to condensed Ca islands. Thus, we calculate the DOS of the close-packed Ca(111) layer on Ag(111) where Ca-Ca bond length is 0.39 nm to explore the origin of the G state in Fig. 4(b) and Figs. S7 and S8 [56]. Similar to the DOS of noninteracting Ca atoms, the 3*d*-orbital character is dominant in the electronic bands of the close-packed Ca(111) layer on Ag(111). The DFT-calculated DOS exhibits a prominent feature with a peak at ∼2.5 eV (see Fig. S7 [56]). Its calculated effective mass of $m_{\mathrm{eff}} = \sim 0.52 m_e$ is in good agreement with the measured value of $(0.47 \pm 0.04) m_e$. This DOS feature is likely associated with the state G of condensed Ca islands. Notably, the calculated DOS shows that the 3*d* orbitals also significantly contribute to the occupied states below E_F. We also observe that the chemical interaction between Ca atoms is primarily composed of 4*s* orbitals with some contribution from $3d_{z^2}$ orbitals below the E_F. Thus, theoretical calculations for single Ca atoms and the close-packed Ca(111) layer on Ag(111) consistently show that the low-lying unoccupied states of Ca have significant 3*d*-orbital character. Although the occupied Ca state is also predicted to have 3*d* character, it nevertheless retains dominant 4*s* electron density that is not transferred to Ag(111).

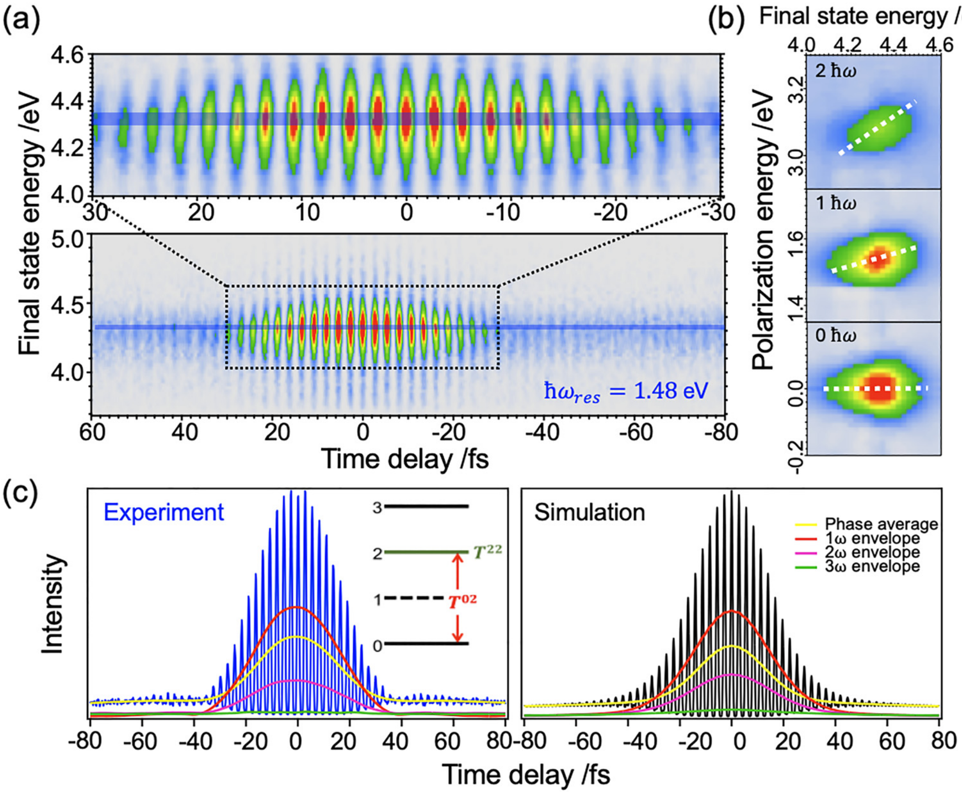

FIG. 5. Interferometric two-pulse correlation (I2PC) measurement. (a) ITR-3PP data for ~0.18 ML Ca/Ag(111) with a photon energy of $\hbar\omega_{\mathrm{res}} = 1.48$ eV at $k_{\parallel} = 0\,\text{Å}^{-1}$. (b) 2D photoelectron spectra obtained by Fourier analysis of interferogram in (a). (c) The experimental I2PC trace (blue, left) is obtained as the horizontal line profile in (a) and its optical Bloch equation simulation (black, right). Inset: Energy diagram for the four-level excitation. The measured signals are decomposed into the phase average (0ω), 1ω, 2ω, and 3ω component envelopes to fit the polarization and population decay parameters [49,89].

C. Ultrafast photoexcitation dynamics

Having established the spectroscopy of Ca on Ag(111), we further explore its photoexcitation dynamics. Specifically, we investigate the electron dynamics following the resonant two-photon photoexcitation state G. We record ITR-3PP interferograms by scanning the delay between identical pump and probe pulses with attosecond precision while recording the energy- and momentum-resolved photoemission spectra related to state G [85]. Figure 5(a) shows a photoemission interferogram of ~0.18 ML Ca on Ag(111) taken with $\hbar\omega_{\mathrm{res}} = 1.48$ eV at $k_{\parallel} = 0\,\text{Å}^{-1}$. The pulse duration (~19 fs) of the ultrafast laser pulse at $\hbar\omega_{\mathrm{res}} = 1.48$ eV is established by interferometric third-order autocorrelation taken by recording the 4PP signal from a polycrystalline Mo sample holder (Fig. S9 [56]). As the delay time increases from 0 fs, the hyperbolic angle tilting of interferometric fringes with respect to the delay time within the magnified image in Fig. 5(a) signifies the induced coherence in the 3PP excitation pathway at the resonance transition [49,86,87]. By Fourier transforming the interferogram, we obtain a more direct signature of coherence in the 3PP process where Fig. 5(b) shows 2D photoelectron spectra, bottom to top, for the zero- ($0\hbar\omega$), first- ($1\hbar\omega$), and second-order ($2\hbar\omega$) polarization frequencies. The zero-order component follows the incoherent population dynamics of excited electron populations, while the first- and second-order components record the linear and second-order nonlinear coherences, respectively. The tilting of $1\hbar\omega$ and $2\hbar\omega$ components confirms that the two-photon transition from state R to state G is a coherent process [49,86]. By taking the horizontal line profile at $E_{\mathrm{fin}} = {\sim}4.33$ eV in Fig. 5(a), we obtain an experimental interferometric two-pulse correlation (I2PC) trace for the resonant excitation in Fig. 5(c). Corresponding simulation with an optical Bloch equation (OBE) approach is also shown in the right-hand panel. Here, we use a four-level 3PP excitation scheme as depicted in the inset, where T^{02} is the coherent dephasing time between states R and G, and T^{22} is the G-state resonance decay time. The colored lines overlapping the experimental and simulated I2PC traces show signal decompositions into the phase average and 1ω, 2ω, and 3ω component envelopes, respectively. The OBE simulations are performed until the calculated envelopes reproduce the experimental ones. The best-fit parameters obtained thereby correspond to a dephasing time (T^{02}) of ~21 fs and a population lifetime (T^{22}) of ~52 fs, respectively. Such a long lifetime is comparable with chemisorbed Cs atoms on noble metal substrates [14,88], suggesting the possibility of coherent manipulation of optoelectronic properties of Ca surfaces. For the comparison, we also perform I2PC measurement at off-resonant excitation ($\hbar\omega = 1.63$ eV) in Fig. S10 [56]. Contrary to resonant excitation, the I2PC trace is comparable with the autocorrelation trace in Fig. S9 [56].

IV. DISCUSSION

The structuring of adsorbates on surfaces is defined by a balance between the adatom substrate and competing electrostatic repulsive or attractive lateral interactions between adsorbates. The STM results in Fig. 2(d) provide the direct evidence for the preferential atomic binding of Ca atoms to substrate steps followed by condensation and growth into 2D islands. The total energy calculations for single Ca atom adsorption on Ag(111) in Fig. S11(a) [56] reveal the adatom-substrate potential with an extremely low diffusion barrier (∼1 meV) through bridge site maxima, suggesting that free diffusion occurs even at 77 K (∼7 meV), and subsequent 2D island condensation starts from step edges or point defects, which apparently have a larger lateral binding energy, explaining the STM finding of step-edge-dominated growth. It is likely that atoms on terraces experience a long-range Coulomb repulsion that suppresses their condensation into islands. Nevertheless, the less pronounced terrace growth can occur if Ca atoms encounter point defects or other Ca atoms to seed island nucleation. Figure S11(b) [56] (upper panel) depicts the potential energy pathway experienced by a single Ca atom as it interacts with decorating Ca atoms along the step edge. The calculated barrier to a bond formation (0.11 eV) is noted to be comparable to the bond strength (0.1 eV), resulting in the formation of the Ca-Ca interatomic bonding at step edges. Furthermore, the potential energy pathway for 2D Ca tetramer formation on Ag(111) (Fig. S11(b) [56], lower panel) confirms that the smaller potential barrier (0.04 eV) and larger bond strength (0.06 eV) for Ca tetramer formation facilitate the subsequent growth of 2D planar structures as Ca coverage increases. This condensation behavior has been predicted to have larger cohesive energy for heavy AE elements such as Ca, Sr, and Ba, as compared with Mg and Be, on account of the d-orbital density near E_F. The consequent cohesive energies of roughly 1 eV [21,90,91] agree with our DFT-calculated value of ∼1.14 eV/Ca atom. Especially in the case of Ca at the threshold between s- and d-block elements, there are no d core states and therefore the d-like states near E_F experience a strong attractive potential leading to a small interatomic distance and a larger cohesion energy compared to Sr and Ba [21]. As shown in Fig. 4 and Figs. S5–S8 [56], our finding that the electronic structure of single-atom and condensed island Ca phases near E_F has significant d-orbital character relative to that of s and p largely explains the condensation behavior and larger cohesive energy for Ca, as compared with alkali-metal atoms [21,92].

With experiment and theory, we have also examined the valence electron charge on single Ca atoms by calculating the partial charge transfer of $\sim 1.2e^-$ for a 6 × 6 overlayer on Ag(111) in Fig. S1 and Table S1 [56]. The remaining 4s electron density can participate in metallic Ca-Ca bonding. As the Ca coverage increases, especially in a condensed Ca island, the valence electron transfer is reduced to $\sim 0.9e^-$ (for a Ca tetramer) due to enhanced interatomic interaction among Ca atoms, which further stabilizes the valence electronic states by promoting charge delocalization. Contrary to alkali-metal-atom chemisorption, where metallization occurs upon condensation at a critical coverage (θ_c) between half a monolayer and two monolayers [7,93], the coverage that favors condensation of Ca at terrace edges is significantly lower (∼0.05 ML), suggesting that it does not involve a coverage-dependent phase transition but a defect-dependent attraction that drives entropy reduction at a low coverage. Similar condensation behavior has been reported for Ca/Cu(100) after $\theta_c \leqslant 0.05$ ML [94]. Therefore, the different aggregation behavior of Ca with respect to chemisorbed alkali-metal atoms is a joint outcome of a small surface corrugation potential, strong d-orbital interaction between adjacent Ca atoms, and weak corrugation atom-substrate interaction. From the observed Ca monolayer condensation, we conclude that the interaction between Ca adatoms and the Ag(111) surface is dominated by mutual ionic interaction, which leads to low corrugation in the adatom-substrate interaction, whereas the Ca-Ca interaction has appreciable covalent d-orbital character.

The weak Ca-Ag(111) interaction persists to dynamics of the G-state electronic dynamics as evidenced by the relatively slow dephasing and population decay at ∼2.7 eV above E_F. Similarly slow electronic relaxation processes have been observed for alkali-metal atoms on noble metals and the Ru(0001) surface. Although the Ca atom retains a 4s electron upon chemisorption, it is unlikely that the photoexcitation process involves interatomic promotion to an excited state, followed by photoemission. The interaction of an electron with the doubly ionized hole charge would likely have a strong transient exciton band profile [85]. Therefore, for both alkali-metal and Ca atoms, the excitation predominantly involves charge transfer excitation where an electron is transferred from the substrate back to the alkali-metal atom. The G state lies within the projected band gap of Ag(111), so the relatively slow decay implies that the electron density is effectively confined to the surface. This is anticipated to be consistent with the d_{xy} character of the unoccupied Y state. The long effective dephasing is further surprising because of the rough step-edge structures, probably caused by strong electron 2D confinement leading to significant inhomogeneous broadening, as can also be surmised from its width in 2PP spectra, as well as site-dependent STS resonances. Given its energy position at ∼0.9 eV below E_{vac} [see Fig. 3(c)], which is near the image potential (IP) state of the Ca island, the G state may hybridize with it. This hybridization could significantly contribute to the observed long dephasing and lifetime because the IP density is delocalized into the vacuum. The excited state lifetimes further suggest that the coupling to the substrate is weak even at step edges. These ultrafast studies suggest that ultrafast photocatalysis on Ca/Ag(111) surfaces where the electronically excited Ca species induce chemistry could be effective.

V. SUMMARY AND CONCLUSIONS

The adsorption of proto-transition-metal Ca on Ag(111) exhibits interesting electronic and structural properties that arise from its intermediate position between alkali metals and transition metals that lends it unique electronic configuration and complex orbital hybridization. Whereas the ”light” alkaline-earth elements, Be and Mg, lacking d orbitals tend to exhibit a neutral or covalent character between anionic and cationic adsorbates akin to He atoms (with closed ns^2 shell configuration) [48], the similarity to the alkali-metal atoms favors ionic chemisorption that engages *d* orbitals in its interatomic interactions.

In this study, we report the diverse electronic properties of Ca atoms that affect its adsorption on a noble metal, Ag(111), surface, by complementary surface-sensitive microscopic and spectroscopic techniques. Using static 3PP spectroscopic measurements, we record the electronic structure of ∼0.18 ML Ca on Ag(111) to find an occupied state R and two unoccupied states G and Y. DFT calculations show that, upon chemisorption, Ca atoms transfer about one 4*s* electron (∼$1.2e^-$ for Ca atom and ∼$0.9e^-$ for Ca tetramer) to the substrate, similar to alkali-metal atoms. Despite this charge transfer ionization, the remaining electron forms the occupied state R near E_F, consistent with Ca still possessing a metallic character even at the smallest coverages. According to DFT calculations, the observed occupied R and unoccupied G states possess significant 3*d*-orbital character. This proto-transition-metal character is probably responsible for Ca forming one-atomic-layer-thick islands where the 3*d*-orbital character favors formation of covalent bonding despite the dipole-dipole repulsion that is common to ionized adsorbates on metal surfaces. The discovery of an occupied state suggests not only the partial charge transfer to the Ag(111) surface, but also the evidence of early-stage metallic condensation of Ca atoms. Additionally, a strong coverage dependence of spectral line FWHM and the spatial-position-dependent STM and STS measurement of the unoccupied state energy G indicates the atomic condensation occurs at a deep submonolayer coverage ($\geqslant$0.05 ML), forming a rugged structure. In contrast to the chemisorbed alkali-metal atoms which adopt a dispersed phase on noble metal surfaces, the early condensation of the Ca atom is explained by a significant involvement of 3*d* orbitals to the electronic structure, which induces the strong 4*s*-3*d* mixing and consequently stabilizes the Ca-Ca bond. Finally, the real-time observation by ITR-3PP spectroscopy of electron dynamics upon two-photon induced resonance reveals a charge transfer to the 3*d* state of the Ca island. Electronic transition by the resonant excitation to the 3*d* state drives the coherent electron excitation with the dephasing time of ∼21 fs and a long lifetime of ∼52 fs, which is comparable to the 5*s* state of Cs on Cu(111) [95–97]. Such a long-lived electronic state of alkali-metal atoms has been found to drive frustrated desorption on account of its Coulomb repulsion with the substrate [96]. Contrary to Cs, chemisorbed Ca on Ag(111) partially transfers its 4*s* valence electron to the substrate. Thus, the photoexcitation likely transfers an electron to the 3*d*-orbital-derived bands of Ca islands. Because of the strong Ca interactions within the islands, the photoexcited electron is probably delocalized over neighboring atoms, as is evident from the free-electron-like G-state dispersion, and therefore does not induce strong adsorbate-substrate repulsion as in the case of single Cs atoms. The delocalization of electrons also likely hinders their decay back to the conduction band of Ag(111) on account of the projected band gap, that inhibits hybridization between adsorbate and substrate bands. Therefore, the observation of photoinduced long-lived resonance involved in 3*d* orbitals provides further evidence supporting the transition-metal-like properties of Ca and offers the possibility to induce and control various photocatalytic processes involving excited electrons, such as the photocatalytic reduction of CO_2 [65,98]. The electron delocalization within the excited state can promote its trapping and chemistry at sites of chemisorption.

ACKNOWLEDGMENT

This research was supported by the National Science Foundation (Grant No. CHE-2303197).

[1] H. P. Bonzel, A. M. Bradshaw, and G. Ertl, *Physics and Chemistry of Alkali Metal Adsorption* (Elsevier, Amsterdam, 1989).

[2] I. Langmuir, The nature of adsorbed films of caesium on tungsten. Part I. The space charge sheath and the image force, Phys. Rev. **43**, 224 (1933).

[3] J. P. Muscat and D. M. Newns, Chemisorption on metals, Prog. Surf. Sci. **9**, 1 (1978).

[4] N. V. Smith and W. E. Spicer, Photoemission studies of the alkali metals. I. Sodium and potassium, Phys. Rev. **188**, 593 (1969).

[5] J. J. Hopfield, Effect of electron-electron interactions on photoemission in simple metals, Phys. Rev. **139**, A419 (1965).

[6] J. W. Gadzuk, J. K. Hartman, and T. N. Rhodin, Approach to alkali-metal chemisorption within the Anderson model, Phys. Rev. B **4**, 241 (1971).

[7] T. Aruga and Y. Murata, Alkali-metal adsorption on metals, Prog. Surf. Sci. **31**, 61 (1989).

[8] J. P. Gauyacq, A. G. Borisov, and M. Bauer, Excited states in the alkali/noble metal surface systems: A model system for the study of charge transfer dynamics at surfaces, Prog. Surf. Sci. **82**, 244 (2007).

[9] N. Fischer, S. Schuppler, T. Fauster, and W. Steinmann, Coverage-dependent electronic structure of Na on Cu(111), Surf. Sci. **314**, 89 (1994).

[10] M. Bauer, S. Pawlik, and M. Aeschlimann, Resonance lifetime and energy of an excited Cs state on Cu(111), Phys. Rev. B **55**, 10040 (1997).

[11] J. Zhao *et al.*, Electronic potential of a chemisorption interface, Phys. Rev. B **78**, 085419 (2008).

[12] G. Butti, S. Caravati, G. P. Brivio, M. I. Trioni, and H. Ishida, Image potential states and electronic structure of Na/Cu(111), Phys. Rev. B **72**, 125402 (2005).

[13] G. P. Brivio, G. Butti, S. Caravati, G. Fratesi, and M. I. Trioni, Theoretical approaches in adsorption: Alkali adatom investigations, J. Phys.: Condens. Matter **19**, 305005 (2007).

[14] S. Zhang, C. Wang, X. Cui, Y. Wang, A. Argondizzo, J. Zhao, and H. Petek, Time-resolved photoemission study of the electronic structure and dynamics of chemisorbed alkali atoms on Ru(0001), Phys. Rev. B **93**, 045401 (2016).

[15] S. Achilli *et al.*, Spectral properties of Cs and Ba on Cu(111) at very low coverage: Two-photon photoemission spectroscopy and electronic structure theory, Phys. Rev. B **80**, 245419 (2009).

[16] A. G. Borisov *et al.*, π Resonance of chemisorbed alkali atoms on noble metals, Phys. Rev. Lett. **101**, 266801 (2008).

[17] S. Achilli, M. I. Trioni, and E. V. Chulkov, Self-consistent approach for spectral properties of single alkali adatoms on Cu(111), Phys. Rev. B **85**, 045408 (2012).

[18] R. Li, H. Ma, X. Cheng, S. Wang, D. Li, Z. Zhang, Y. Li, and X.-Q. Chen, Dirac node lines in pure alkali earth metals, Phys. Rev. Lett. **117**, 096401 (2016).

[19] A. Seidu, A. Marini, and M. Gatti, Dynamical correlation effects in a weakly correlated material: Inelastic x-ray scattering and photoemission spectra of beryllium, Phys. Rev. B **97**, 125144 (2018).

[20] R. A. Bartynski, E. Jensen, T. Gustafsson, and E. W. Plummer, Angle-resolved photoemission investigation of the electronic structure of Be: Surface states, Phys. Rev. B **32**, 1921 (1985).

[21] E. Wimmer, All-electron local density functional study of metallic monolayers. II. Alkaline-earth metals, J. Phys. F. **14**, 681 (1984).

[22] S. Heguri, N. Kawade, T. Fujisawa, A. Yamaguchi, A. Sumiyama, K. Tanigaki, and M. Kobayashi, Superconductivity in the graphite intercalation compound BaC_6, Phys. Rev. Lett. **114**, 247201 (2015).

[23] J. S. Kim, L. Boeri, J. R. O'Brien, F. S. Razavi, and R. K. Kremer, Superconductivity in heavy alkaline-earth intercalated graphites, Phys. Rev. Lett. **99**, 027001 (2007).

[24] S. Ichinokura, K. Sugawara, A. Takayama, T. Takahashi, and S. Hasegawa, Superconducting calcium-intercalated bilayer graphene, ACS Nano **10**, 2761 (2016).

[25] G. Csányi, P. B. Littlewood, A. H. Nevidomskyy, C. J. Pickard, and B. D. Simons, The role of the interlayer state in the electronic structure of superconducting graphite intercalated compounds, Nat. Phys. **1**, 42 (2005).

[26] M. Ziegler, J. Kröger, R. Berndt, A. Filinov, and M. Bonitz, Scanning tunneling microscopy and kinetic Monte Carlo investigation of cesium superlattices on Ag(111), Phys. Rev. B **78**, 245427 (2008).

[27] C. J. Todd and T. N. Rhodin, Adsorption of single alkali atoms on tungsten using field emission and field desorption, Surf. Sci. **42**, 109 (1974).

[28] J. Ren, Y. Wang, J. Zhao, S. Tan, and H. Petek, K atom promotion of O_2 chemisorption on Au(111) surface, J. Am. Chem. Soc. **141**, 4438 (2019).

[29] J. Ellis, A. P. Graham, F. Hofmann, and J. P. Toennies, Coverage dependence of the microscopic diffusion of Na atoms on the Cu(001) surface: A combined helium atom scattering experiment and molecular dynamics study, Phys. Rev. B **63**, 195408 (2001).

[30] L. Aballe, A. Barinov, A. Locatelli, T. O. Mentes, and M. Kiskinova, Initial stages of heteroepitaxial Mg growth on W(110): Early condensation, anisotropic strain, and self-organized patterns, Phys. Rev. B **75**, 115411 (2007).

[31] O. M. Braun and V. K. Medvedev, Interaction between particles adsorbed on metal surfaces, Sov. Phys. Usp. **32**, 328 (1989).

[32] Z. A. Ibrahim and M. J. G. Lee, Surface electronic structures of Ba overlayers on W(100), W(110), and W(111), Phys. Rev. B **76**, 155423 (2007).

[33] V. A. Sashin, M. A. Bolorizadeh, A. S. Kheifets, and M. J. Ford, Electronic band structure of metallic calcium measured by electron momentum spectroscopy, J. Phys.: Condens. Matter **12**, 9407 (2000).

[34] K. A. Kress and G. J. Lapeyre, Photoemission measurement of the d-band energies in calcium, Solid State Commun. **9**, 827 (1971).

[35] X. Wu, L. Zhao, J. Jin, S. Pan, W. Li, X. Jin, G. Wang, M. Zhou, and G. Frenking, Observation of alkaline earth complexes $M(CO)_8$ ($M =$ Ca, Sr, or Ba) that mimic transition metals, Science **361**, 912 (2018).

[36] Q. Wang, S. Pan, S. Lei, J. Jin, G. Deng, G. Wang, L. Zhao, M. Zhou, and G. Frenking, Octa-coordinated alkaline earth metal–dinitrogen complexes $M(N_2)_8$ ($M =$ Ca, Sr, Ba), Nat. Commun. **10**, 3375 (2019).

[37] A. Politano, V. Formoso, and G. Chiarello, Electronic properties of metallic bilayers deposited on Cu(111): A comparative study, Surf. Sci. **603**, 933 (2009).

[38] M. Kaupp, "Non-VSEPR" structures and bonding in d^0 systems, Angew. Chem. Int. Ed. **40**, 3534 (2001).

[39] L. Gagliardi and P. Pyykkö, Cesium and barium as honorary d elements: CsN_7Ba as an example, Theor. Chem. Acc. **110**, 205 (2003).

[40] M. Zhou and G. Frenking, Transition-metal chemistry of the heavier alkaline earth atoms Ca, Sr, and Ba, Acc. Chem. Res. **54**, 3071 (2021).

[41] X. Wu, L. Zhao, D. Jiang, I. Fernández, R. Berger, M. Zhou, and G. Frenking, Barium as honorary transition metal in action: Experimental and theoretical Study of $Ba(CO)^+$ and $Ba(CO)^-$, Angew. Chem. Int. Ed. **57**, 3974 (2018).

[42] K. M. Fromm, Chemistry of alkaline earth metals: It is not all ionic and definitely not boring! Coord. Chem. Rev. **408**, 213193 (2020).

[43] T. Bettens, S. Pan, F. De Proft, G. Frenking, and P. Geerlings, Alkaline earth metals activate N_2 and CO in cubic complexes just like transition metals: A conceptual density functional theory and energy decomposition analysis study, Chem. Eur. J. **26**, 12785 (2020).

[44] J. C. G. Walker, P. B. Hays, and J. F. Kasting, A negative feedback mechanism for the long-term stabilization of Earth's surface temperature, J. Geophys. Res. Oceans **86**, 9776 (1981).

[45] A. Ridgwell and R. E. Zeebe, The role of the global carbonate cycle in the regulation and evolution of the Earth system, Earth Planet. Sci. Lett. **234**, 299 (2005).

[46] M. Hirayama, R. Okugawa, T. Miyake, and S. Murakami, Topological Dirac nodal lines and surface charges in fcc alkaline earth metals, Nat. Commun. **8**, 14022 (2017).

[47] J. Barth, I. Chorkendorff, F. Gerken, C. Kunz, R. Nyholm, J. Schmidt-May, and G. Wendin, $3p$ resonance photoionization of the valence band in metallic Ca: Atomic and solid-state many-body effects, Phys. Rev. B **30**, 6251 (1984).

[48] S. Holmström, Chemisorption of group IIA elements, Phys. Scr. **36**, 529 (1987).

[49] M. Reutzel, A. Li, and H. Petek, Coherent two-dimensional multiphoton photoelectron spectroscopy of metal surfaces, Phys. Rev. X. **9**, 011044 (2019).

[50] G. Kresse and J. Furthmüller, Efficient iterative schemes for *ab initio* total-energy calculations using a plane-wave basis set, Phys. Rev. B **54**, 11169 (1996).

[51] G. Kresse and J. Furthmüller, Efficiency of *ab-initio* total energy calculations for metals and semiconductors using a plane-wave basis set, Comput. Mater. Sci. **6**, 15 (1996).

[52] J. P. Perdew, K. Burke, and M. Ernzerhof, Generalized gradient approximation made simple, Phys. Rev. Lett. **77**, 3865 (1996).

[53] P. E. Blöchl, Projector augmented-wave method, Phys. Rev. B **50**, 17953 (1994).

[54] M. Reutzel, A. Li, B. Gumhalter, and H. Petek, Nonlinear plasmonic photoelectron response of Ag(111), Phys. Rev. Lett. **123**, 017404 (2019).

[55] M. Reutzel, A. Li, and H. Petek, Above-threshold multiphoton photoemission from noble metal surfaces, Phys. Rev. B **101**, 075409 (2020).

[56] See Supplemental Material at http://link.aps.org/supplemental/10.1103/PhysRevB.110.075404 for an analysis of the work function change upon Ca evaporation, angle-resolved 3PP spectra, LDOS characterization by STS measurement, DFT-calculated DOS of Ca on Ag(111), ITR-3PP measurement at off-resonant excitation, and the total energy change upon Ca adsorption on Ag(111). It also contains Refs. [57–64].

[57] L. A. Bol'shov, A. P. Napartovich, A. G. Naumovets, and A. G. Fedorus, Submonolayer films on the surface of metals, Sov. Phys. Usp. **20**, 432 (1977).

[58] R. D. Diehl and R. McGrath, Structural studies of alkali metal adsorption and coadsorption on metal surfaces, Surf. Sci. Rep. **23**, 43 (1996).

[59] J. Zhu, J. A. Farmer, N. Ruzycki, L. Xu, C. T. Campbell, and G. Henkelman, Calcium adsorption on MgO(100): Energetics, structure, and role of defects, J. Am. Chem. Soc. **130**, 2314 (2008).

[60] A. Stenborg and E. Bauer, Two-dimensional Yb on a Mo(110) surface, Phys. Rev. B **36**, 5840 (1987).

[61] L. Romaner, G. Heimel, C. Ambrosch-Draxl, and E. Zojer, The dielectric constant of self-assembled monolayers, Adv. Funct. Mater. **18**, 3999 (2008).

[62] P. Senet, J. P. Toennies, and G. Witte, Low-frequency vibrations of alkali atoms on Cu(001), Chem. Phys. Lett. **299**, 389 (1999).

[63] M. I. Trioni, S. Achilli, and E. V. Chulkov, Key ingredients of the alkali atom–metal surface interaction: Chemical bonding versus spectral properties, Prog. Surf. Sci. **88**, 160 (2013).

[64] S. Sakamoto, G. J. White, K. Kawaguchi, M. Ohishi, K. S. Usuda, and T. Hasegawa, A search for absorption of Mg and Ca compounds in molecular clouds towards Galactic continuum sources, Mon. Not. R. Astron. Soc. **301**, 872 (1998).

[65] D. Ochs, B. Braun, W. Maus-Friedrichs, and V. Kempter, CO_2 chemisorption at Ca and CaO surfaces: A study with MIES, UPS(HeI) and XPS, Surf. Sci. **417**, 406 (1998).

[66] H. Kawano, Effective work functions of the elements: Database, most probable value, previously recommended value, polycrystalline thermionic contrast, change at critical temperature, anisotropic dependence sequence, particle size dependence, Prog. Surf. Sci. **97**, 100583 (2022).

[67] H. Petek, A. Li, X. Li, S. Tan, and M. Reutzel, Plasmonic decay into hot electrons in silver, Prog. Surf. Sci. **98**, 100707 (2023).

[68] L.-M. Wang, V. Sametoglu, A. Winkelmann, J. Zhao, and H. Petek, Two-photon photoemission study of the coverage-dependent electronic structure of chemisorbed alkali atoms on a Ag(111) surface, J. Phys. Chem. A **115**, 9479 (2011).

[69] V. Sametoglu, Ph.D. dissertation, University of Pittsburgh, 2009.

[70] D. A. Arena, F. G. Curti, and R. A. Bartynski, Unoccupied electronic states of the Cs/Cu(100) and Cs/Cu(111) adsorption systems, Phys. Rev. B **56**, 15404 (1997).

[71] J. W. Mirick, C.-H. Chien, and E. Blaisten-Barojas, Electronic structure of calcium clusters, Phys. Rev. A **63**, 023202 (2001).

[72] I. N. Yakovkin, Metallization of the monolayer Mg film with a linear atomic structure, Surf. Sci. **406**, 57 (1998).

[73] R. D. Diehl and R. McGrath, Current progress in understanding alkali metal adsorption on metal surfaces, J. Phys.: Condens. Matter **9**, 951 (1997).

[74] T. von Hofe, J. Kröger, and R. Berndt, Adsorption geometry of Cu(111)-Cs studied by scanning tunneling microscopy, Phys. Rev. B **73**, 245434 (2006).

[75] W. C. Fan and A. Ignatiev, Ordered phases and phase transitions of cesium on the Cu(111) surface, J. Vac. Sci. Technol. A **6**, 735 (1988).

[76] Y. Wang *et al.*, Observing atomic collapse resonances in artificial nuclei on graphene, Science **340**, 734 (2013).

[77] C. Pettersen, A. O. Sjåstad, and O. Ivashenko, Near-surface alloys of PtRh on Rh(111) and Pt(111) characterized by STM, J. Phys. Chem. C **125**, 25140 (2021).

[78] S. Beckord, A. K. Engstfeld, S. Brimaud, and R. J. Behm, Electrochemical characterization and stability of $Ag_xPt_{1-x}/Pt(111)$ surface alloys, J. Phys. Chem. C **120**, 16179 (2016).

[79] H. Röder, R. Schuster, H. Brune, and K. Kern, Monolayer-confined mixing at the Ag-Pt(111) interface, Phys. Rev. Lett. **71**, 2086 (1993).

[80] H. Ueba and B. Gumhalter, Theory of two-photon photoemission spectroscopy of surfaces, Prog. Surf. Sci. **82**, 193 (2007).

[81] D. B. Dougherty, P. Maksymovych, J. Lee, M. Feng, H. Petek, and J. T. Yates, Tunneling spectroscopy of Stark-shifted image potential states on Cu and Au surfaces, Phys. Rev. B **76**, 125428 (2007).

[82] A. Politano, V. Formoso, and G. Chiarello, Annealing effects on the plasmonic excitations of metal/metal interfaces, Appl. Surf. Sci. **255**, 6038 (2009).

[83] J. A. Moriarty, Hybridization and the fcc-bcc phase transitions in calcium and strontium, Phys. Rev. B **8**, 1338 (1973).

[84] A. Politano, Electronic properties of calcium ultrathin layers on Cu(111): A high-resolution electron energy loss spectroscopy study, Surf. Rev. Lett. **17**, 411 (2010).

[85] X. Cui, C. Wang, A. Argondizzo, S. Garrett-Roe, B. Gumhalter, and H. Petek, Transient excitons at metal surfaces, Nat. Phys. **10**, 505 (2014).

[86] A. P. Heberle, J. J. Baumberg, and K. Köhler, Ultrafast coherent control and destruction of excitons in quantum wells, Phys. Rev. Lett. **75**, 2598 (1995).

[87] J. Mauritsson *et al.*, Attosecond electron spectroscopy using a novel interferometric pump-probe technique, Phys. Rev. Lett. **105**, 053001 (2010).

[88] S. Ogawa, H. Nagano, and H. Petek, Phase and energy relaxation in an antibonding surface state: Cs/Cu(111), Phys. Rev. Lett. **82**, 1931 (1999).

[89] M. J. Weida, S. Ogawa, H. Nagano, and H. Petek, Ultrafast interferometric pump–probe correlation measurements in systems with broadened bands or continua, J. Opt. Soc. Am. B **17**, 1443 (2000).

[90] P. A. Dowben, The metallicity of thin films and overlayers, Surf. Sci. Rep. **40**, 151 (2000).

[91] I. N. Yakovkin, Non-metal-to-metal transition in alkaline earth monolayers, Surf. Sci. **442**, 431 (1999).

[92] E. Wimmer, All-electron local density functional study of metallic monolayers. I. Alkali metals, J. Phys. F. **13**, 2313 (1983).

[93] E. W. Plummer and P. A. Dowben, When are thin films of metals metallic? Prog. Surf. Sci. **42**, 201 (1993).

[94] P. Rudolf, C. Astaldi, A. Bianco, and S. Modesti, Ca chemisorption on Cu(100) in the submonolayer regime: Metastable and stable adsorption phases, Phys. Rev. B **47**, 4123 (1993).

[95] H. Petek, H. Nagano, M. J. Weida, and S. Ogawa, Surface femtochemistry: Frustrated desorption of alkali atoms from noble metals, J. Phys. Chem. B **105**, 6767 (2001).

[96] H. Petek and S. Ogawa, Surface femtochemistry: Observation and quantum control of frustrated desorption of alkali atoms from noble metals, Annu. Rev. Phys. Chem. **53**, 507 (2002).

[97] H. Petek, M. J. Weida, H. Nagano, and S. Ogawa, Real-time observation of adsorbate atom motion above a metal surface, Science **288**, 1402 (2000).

[98] X. Dong, L. Wang, G. Wang, and M. Zhou, Carbon dioxide activation by alkaline-earth metals: Formation and spectroscopic characterization of $OCMCO_3$ and MC_2O_4 ($M =$ Ca, Sr, Ba) in solid neon, J. Phys. Chem. A **126**, 4598 (2022).